Elimination of MHD current sheets by modifications to the plasma wall in a fixed boundary model

E. Kim,[1] G.B. McFadden,[2] and A.J. Cerfon[1]

[1]Courant Institute of Mathematical Sciences, NYU, New York, NY 10012

[2]Applied and Computational Mathematics Division, NIST, Gaithersburg, MD 20879

May 18, 2020

Abstract

Models of magnetohydrodynamic (MHD) equilibia that for computational convenience assume the existence of a system of nested magnetic flux surfaces tend to exhibit singular current sheets. These sheets are located on resonant flux surfaces that are associated with rational values of the rotational transform. We study the possibility of eliminating these singularities by suitable modifications of the plasma boundary, which we prescribe in a fixed boundary setting. We find that relatively straightforward iterative procedures can be used to eliminate weak current sheets that are generated at resonant flux surfaces by the nonlinear interactions of resonating wall harmonics. These types of procedures may prove useful in the design of fusion devices with configurations that enjoy improved stability and transport properties.

Keywords: magnetohydrodynamic equilibria; nested flux surfaces; singular current sheets; rational rotational transform; nonlinear mode coupling

1 Introduction

We describe a modification of the magnetohydrodynamic (MHD) equilibrium and stability code NSTAB [24] in order to study the effect of wall perturbations on resonant flux surfaces where singular current sheets are often observed. NSTAB (and our modified version of NSTAB) solves the governing equations

$$\mathbf{J} \times \mathbf{B} = \nabla p, \quad \mathbf{J} = \nabla \times \mathbf{B}, \quad \nabla \cdot \mathbf{B} = 0, \tag{1}$$

where $\mathbf{B}$ is the magnetic field, $\mathbf{J}$ is the current density, p is the plasma pressure, and to simplify the notation we normalized the magnetic permeability to unity. The first equation in (1) is the basic force balance in the plasma, the second defines the current density, and the third expresses the solenoidal nature of the magnetic field.

NSTAB is a fixed boundary code, meaning that the plasma boundary ∂V of the toroid plasma volume V is considered to be given with a prescribed shape. NSTAB equilibria are stationary points of the energy functional [12, 20, 24]

$$E = \int_V \left\{ \frac{|\mathbf{B}|^2}{2} - p \right\} dV, \tag{2}$$

which is extremized over solenoidal fields $\mathbf{B}$ that have vanishing normal flux at the boundary of V. Following [2, 3, 4, 16, 24], an assumption of *nested flux surfaces* is used in formulating the model, and the problem is recast as a variational principle over a class of functions that satisfy this constraint. Although the assumption of nested flux surfaces provides significant computational advantages, the price to be paid is that this assumption can introduce singularities in the solution [6, 7, 21, 23], as will be discussed in some detail.

To implement the constraint of nested flux surfaces the toroidal flux itself is introduced as an independent variable, and the variational principle is posed in a fixed computational domain that is defined in terms of the independent variables (s, u, v) in a unit cube. Here s is the normalized toroidal flux with $0 < s < 1$, and u and v are normalized poloidal and toroidal angles. Since $\mathbf{B} \cdot \nabla p = 0$, the pressure is constant on an ergodic flux surface,

and the problem formulation is completed by prescribing the pressure field $p(s)$ and the rotational transform $\iota(s)$ (see, e.g., [1]) as functions of the flux label s. The rotational transform ι is a measure of the average number of poloidal turns a magnetic field line makes during each toroidal turn around the flux surface. It can also be expressed as the derivative of the poloidal flux with respect to the toroidal flux [14].

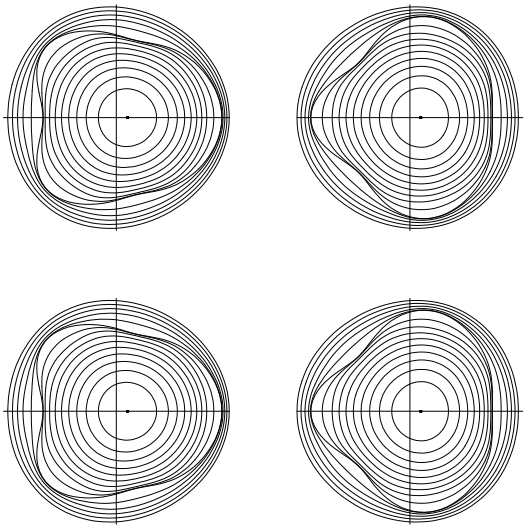

Figure 1: NSTAB computation of four cross-sections of a torus with aspect ratio $A = 5$. From left to right and top to bottom, the normalized toroidal angles are $v = 0$, $v = 1/4$, $v = 1/2$ and $v = 3/4$. The pressure is given by $p(s) = 0.01(1 - s^2)^2$, and the rotational transform is $\iota(s) = 0.6{+}0.1s$. The observed spacing of the displayed flux surfaces (contours of constant s) reflects a singular current sheet that occurs at a resonant flux surface where $\iota(s) = 2/3$, and the surfaces display a corresponding symmetry with poloidal and toroidal mode numbers $(m, n) = (3, 2)$.

The singularities in this model tend to occur on so-called *resonant flux surfaces* where the rotational transform assumes rational values, $\iota(s) = n/m$. These singularities can be interpreted as current sheets located at the resonant flux surfaces which are present to prevent the formation of islands that would otherwise develop in an equilibrium without the constraint of nested flux surfaces [21]. An example of an NSTAB calculation with

current sheets is shown in Fig. 1, where the flux surfaces alternately bunch up and spread out around a resonant surface where $\iota(s) = 2/3$. The $(3, 2)$ symmetry of the resonance is clear in the cross-sections of the flux surfaces at four stations around the torus, and the local distortions occur at points where the Jacobian $\partial(x, y, z)/\partial(s, u, v)$ of the mapping from computational to physical coordinates assumes large or small values. These local distortions are representative of the tendency of the equilibrium to allow for magnetic islands, if the constraint of nested flux surfaces were relaxed [13]. The relation between the singular current sheet, as reflected in the behavior of the mapping Jacobian, and the prescribed wall geometry is the subject of this study, which will be conducted numerically in a simplified geometry. A detailed theoretical discussion of the underlying differential equations requires the machinery of KAM theory [8] which hinges upon the occurrence of "small divisors" in the problem. These present significant numerical issues for convergence under mesh refinement; here we will confine our attention to the numerical treatment of the underlying discretized model in which the problem of small divisors is sidestepped by restricting the degrees of freedom in the angular coordinates [6].

Desirable MHD equilibria with good particle confinement typically feature a large fraction of the plasma volume with nested flux surfaces, and few, narrow magnetic islands with correspondingly small regions with magnetic field stochasticity surrounding them. A corresponding NSTAB equilibrium would exhibit only weak current sheets at resonant surfaces. In this paper, we explore the possibility of prescribing the shape of the fixed plasma boundary in such a way that resonant singularities are suppressed. To do so, we have examined a modified form of NSTAB that is suitable for a slab geometry, in a doubly-periodic domain that is bounded by two given flux surfaces. We chose to consider this simplified geometry, corresponding to a topological torus without the curvature effects of a true torus, in order to avoid complications associated with the magnetic axis [2, 3, 4, 24, 25] that is surrounded by the innermost flux surface in a toroidal geometry, which represents a coordinate singularity requiring special numerical treatment. Our work is motivated by the recent analysis of Weitzner [25], which suggests that one can tailor the

outermost flux surface in order to avoid resonance-induced singularities. The present study shares many similarities with the recent work of Mikhailov, Nührenberg and Zille [23], with the following notable differences. Mikhailov *et al.* remove singularities in true toroidal stellarator equilibria computed with VMEC [16], as opposed to the slab geometry in the present work. On the other hand, we will show that we can adjust the outermost flux surface in order to remove singularities at multiple resonant flux surfaces, whereas Mikhailov *et al.* only focused on the removal of a single singularity. In addition, we demonstrate that the method also applies to equilibria with pressure profiles with a finite pressure gradient throughout the plasma volume, whereas in their work based on VMEC equilibria, Mikhailov *et al.* flattened the pressure profile in the neighborhood of the resonant flux surface before removing the current sheet through an appropriate boundary perturbation.

Our work is also distinct from strategies which modify the shapes of the coils [10, 19, 26] or directly the amplitudes of the components of the vacuum field [9] to increase the fraction of the plasma volume which has nested flux surfaces, and reduce the size of magnetic islands. This line of research requires free boundary calculations and equilibrium solvers which do not a priori assume the existence of a full set of nested flux surfaces. It has long been recognized that a "one-step" stellarator optimization process, in which one designs a stellarator by directly designing the coils, can be desirable, since engineering constraints can be included quite naturally in the optimization procedure, and the magnetic field configuration one obtains at the end of the optimization process is then automatically compatible with reasonable coil shapes. However, stellarators have been historically designed with "two-step" optimization strategies, in which one first optimizes the stellarator starting from fixed boundary equilibria, and then, in a second step, optimizes for coils necessary to achieve such equilibria. The "two-step" method remains often favored to this day, because free-boundary computations are more expensive than fixed-boundary computations, and because it has been empirically observed that it more readily gives equilibria with a reasonably large set of nested flux surfaces from the

outset. The work we present here is directly applicable to the "two-step" optimization strategy. Furthermore, as we discussed previously, since we use an equilibrium solver which assumes the existence of nested flux surfaces throughout the plasma volume, we do not directly measure the quality of the equilibria through the approximate calculation of islands widths and the visualization and measure of magnetic stochasticity, unlike in [9, 10, 19, 26]. Instead, we estimate the quality of an equilibrium by the smoothness of the parallel current and the Jacobian of the mapping in the neighborhood of rational surfaces. Our approach has the advantage of numerical efficiency and robustness, since equilibrium codes assuming nested flux surfaces are significantly faster and tend to have more robust convergence properties.

The structure of this article is as follows. In the next section, we present the formulation for the slab version of NSTAB, which we have called NSLAB. In the following section, we derive a linearized model starting from the NSLAB formulation, in which the singularity at resonant flux surfaces appears explicitly. We then present numerical results for the full set of nonlinear governing equations, and end the article with some conclusions and suggestions for future work.

2 A slab version of NSTAB: NSLAB

2.1 Governing equations

We describe a modification of the stellarator equilibrium code NSTAB [24], denoted "NSLAB," that solves the governing equations (1) in a topological torus, or slab geometry, allowing us to avoid dealing with the magnetic axis that occurs in a toroidal geometry. The physical domain is assumed to be doubly periodic in x and y, which play the role of the "poloidal" and "toroidal" angles in this simplified geometry. The fields have periods L_x and L_y, with $x = L_x u$ and $y = L_y v$, where $0 \leq u \leq 1$ and $0 \leq v \leq 1$. The mapping to physical space $\mathbf{x} = \mathbf{x}(s, u, v)$ is given by

$$x = L_x u, \quad y = L_y v, \quad z = z_0(u, v) + R(s, u, v)[z_1(u, v) - z_0(u, v)], \tag{3}$$

where $z_0(u,v)$ and $z_1(u,v)$ are the coordinates of the lower and upper flux surfaces, corresponding to $s=0$ and $s=1$, respectively, with $R(0,u,v)=0$ and $R(1,u,v)=1$, and where we follow the dimensionless treatment of the governing equations used in NSTAB [24], wherein the characteristic length scale is given by the minor radius. The monotonicity of $R(s,u,v)$ as a function of s incorporates the assumed constraint of nested flux surfaces. In physical space, the flux surfaces are the graphs of the function $z(s,u,v)$ as a function of u and v for constant s.

The solenoidal magnetic field $\mathbf{B}(s,u,v)$ is represented in terms of a Clebsch potential $\psi(s,u,v)$ as

$$\mathbf{B} = \nabla\psi \times \nabla s = B^u \mathbf{t}_u + B^v \mathbf{t}_v, \tag{4}$$

where the contravariant basis vectors are

$$\mathbf{t}_u = \frac{\partial \mathbf{x}}{\partial u} = L_x \widehat{\mathbf{x}} + \left[\frac{\partial z_0}{\partial u} + R\left(\frac{\partial z_1}{\partial u} - \frac{\partial z_0}{\partial u} \right) + (z_1 - z_0) \frac{\partial R}{\partial u} \right] \widehat{\mathbf{z}}, \tag{5}$$

$$\mathbf{t}_v = \frac{\partial \mathbf{x}}{\partial v} = L_y \widehat{\mathbf{y}} + \left[\frac{\partial z_0}{\partial v} + R\left(\frac{\partial z_1}{\partial v} - \frac{\partial z_0}{\partial v} \right) + (z_1 - z_0) \frac{\partial R}{\partial v} \right] \widehat{\mathbf{z}}, \tag{6}$$

$$\mathbf{t}_s = \frac{\partial \mathbf{x}}{\partial s} = (z_1 - z_0) \frac{\partial R}{\partial s} \widehat{\mathbf{z}}. \tag{7}$$

Here $\widehat{\mathbf{x}}$, $\widehat{\mathbf{y}}$, and $\widehat{\mathbf{z}}$ are unit vectors in the x, y, and z directions. The Jacobian of the coordinate transformation is given by

$$J(s,u,v) = \frac{\partial(x,y,z)}{\partial(s,u,v)} = \mathbf{t}_s \cdot \mathbf{t}_u \times \mathbf{t}_v = L_x L_y \left[z_1(u,v) - z_0(u,v) \right] \frac{\partial R}{\partial s}(s,u,v), \tag{8}$$

and the contravariant components of $\mathbf{B}$ are

$$B^u(s,u,v) = \frac{1}{J} \frac{\partial \psi}{\partial v}(s,u,v), \quad B^v(s,u,v) = -\frac{1}{J} \frac{\partial \psi}{\partial u}(s,u,v). \tag{9}$$

We observe that since Eq. (4) may also be written as $\mathbf{B} = \nabla \times (\psi \nabla s)$, we may interpret ψ as the s-component of a covariant vector potential $\mathbf{A} = \psi \nabla s$, so that the corresponding current density is $\mathbf{J} = \nabla \times [\nabla \times (\psi \nabla s)]$.

With this representation, the dependent variables in NSLAB are $R(s,u,v)$ and $\psi(s,u,v)$, which satisfy partial differential equations that result from the the first variation of the

energy (2),

$$0 = \delta E = \iiint \left[L_1(\psi)\delta\psi + L_2(R)\delta R \right] \, \mathrm{d}s \, \mathrm{d}u \, \mathrm{d}v. \tag{10}$$

The Euler-Lagrange equations $L_1(\psi) = 0$ and $L_2(R) = 0$ can be written in the form [24]

$$L_1(\psi) = \frac{\partial B_u}{\partial v} - \frac{\partial B_v}{\partial u} = 0 \tag{11}$$

$$L_2(R) = \frac{\partial \psi}{\partial u}\left[\frac{\partial B_s}{\partial v} - \frac{\partial B_v}{\partial s}\right] - \frac{\partial \psi}{\partial v}\left[\frac{\partial B_s}{\partial u} - \frac{\partial B_u}{\partial s}\right] + p'(s)J = 0. \tag{12}$$

These equations are expressed in terms of the covariant components of $\mathbf{B}$,

$$\mathbf{B} = B_s \nabla s + B_u \nabla u + B_v \nabla v, \tag{13}$$

where

$$B_s = \mathbf{t}_s \cdot \mathbf{B}, \quad B_u = \mathbf{t}_u \cdot \mathbf{B}, \quad B_v = \mathbf{t}_v \cdot \mathbf{B}. \tag{14}$$

We note that the current density $\mathbf{J} = \nabla \times \mathbf{B}$ can be written as

$$\mathbf{J} = J^s \mathbf{t}_s + J^u \mathbf{t}_u + J^v \mathbf{t}_v, \tag{15}$$

where the contravariant components of $\mathbf{J}$ are

$$J^s = \frac{1}{J}\left(\frac{\partial B_v}{\partial u} - \frac{\partial B_u}{\partial v}\right), \quad J^u = \frac{1}{J}\left(\frac{\partial B_s}{\partial v} - \frac{\partial B_v}{\partial s}\right), \quad J^v = \frac{1}{J}\left(\frac{\partial B_u}{\partial s} - \frac{\partial B_s}{\partial u}\right). \tag{16}$$

These expressions give us clear interpretations for Eq. (11) and Eq. (12). Eq. (11) expresses the fact that the force balance condition $\mathbf{J} \times \mathbf{B} = \nabla p$ implies that $J^s = \mathbf{J} \cdot \nabla s = 0$. Eq. (12) is the s-component of the force balance (expressed in covariant form).

We denote by $Jp(s, u, v)$ the quantity

$$Jp = \frac{\mathbf{J} \cdot \mathbf{B}}{|\mathbf{B}|^2} = \frac{J^u B_u + J^v B_v}{|\mathbf{B}|^2}, \quad |\mathbf{B}|^2 = B^u B_u + B^v B_v. \tag{17}$$

In a slight abuse of vocabulary, for the remainder of the article we will simply refer to Jp as the parallel current, although the actual parallel current density has instead a single power of $|\mathbf{B}|$ in the denominator (see, e.g., Section 2.7 of Reference [15]).

We note that the analysis of current sheets is often facilitated by the use of special coordinate systems, such as the one developed by Boozer (see, e.g., [14]), in which the magnetic field lines are straight. Fourier analysis in such coordinates then reveals that the resonant Fourier component of the parallel current is in general the sum of two singular terms: the first term exhibits a delta-function-like singularity, and the second term a "$1/x$" or pole singularity [14, 23]. These results are useful in interpreting the singularities that we observe in our NSLAB computations; nevertheless, since our numerical scheme does not employ a straight field line coordinate system, our observed singularities with nested flux surfaces can differ quantitatively from these results. Even so, in the slab geometry with small-amplitude wall perturbations which we mostly focus on here, our computed parallel current profiles on discrete meshes tend to resemble delta-function-like profiles at rational surfaces, and the pole singularities are not observed. However, we have verified that, for very large values of β or more distorted wall geometries, such as the equilibrium shown in Figure 2, solutions with pole singularities can be observed with NSLAB. These more complex cases are beyond the scope of this study, but are the subject of ongoing detailed analysis, with results to be communicated at a later date.

Following the normalization for $\psi(s,u,v)$ adopted in [24], we write

$$\psi(s,u,v) = \pi[u - \iota(s)v] + \tilde{\psi}(s,u,v), \tag{18}$$

where $\tilde{\psi}$ is periodic in u and v. Although ψ is multi-valued, from Eq. (4) this representation leads to a single-valued magnetic field with poloidal and toroidal fluxes determined by the rotational transform $\iota(s)$. We also note that Eq. (11) determines $\tilde{\psi}$ only up to an arbitrary function of s, which we specify by requiring the mean Fourier harmonic $\tilde{\psi}_{00}(s)$ to vanish.

2.2 Numerical Scheme

The nonlinear governing equations (11) and (12) are solved numerically following the procedure given in [24]. In brief, the equations are discretized using second-order-accurate

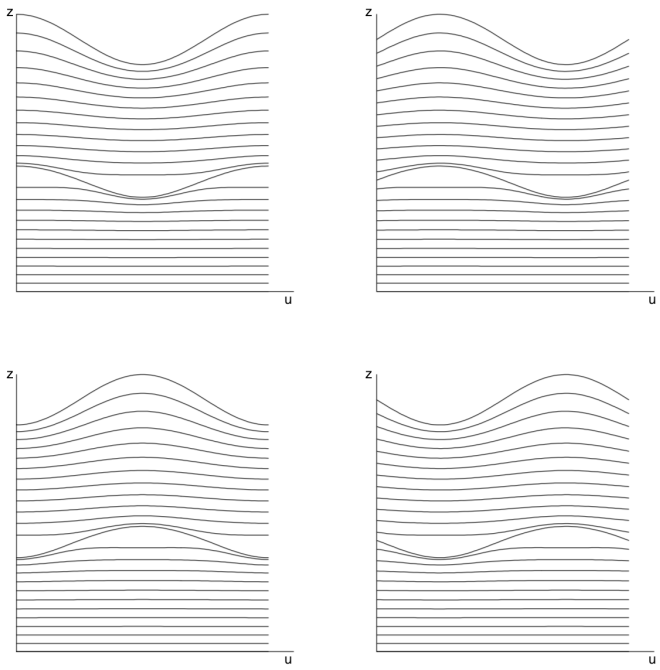

Figure 2: NSLAB computation of a slab equilibrium as described in section 2, for $L_x = L_y = 1$, the pressure profile $p(s) = 0.01(1 - s^2)^2$, the rotational transform profile $\iota(s) = 0.5 + 1.0s$, a flat lower flux surface, $z_0(u, v) = 0$, and an upper flux surface given by $z_1(u, v) = 1 + 0.1 \cos 2\pi(u - v)$. The plots show various flux surfaces $z = z(s, u, v)$ for constant s versus the poloidal angle u at four toroidal angles $v = 0$, $v = 1/4$, $v = 1/2$, and $v = 3/4$ (from left to right and from top to bottom).

finite differences in s, with a pseudospectral representation in the angular variables u and v. A staggered mesh in s is employed, with $L_2(R)$ evaluated at nodes, and $L_1(\psi)$ evaluated at centers; this allows a conservative difference scheme with a compact stencil [2] that can capture singularities over two or three mesh points, as illustrated in the numerical results below.

A second-order Richardson method is used to solve the resulting equations iteratively. This scheme can be viewed as introducing an artificial time t, and solving

$$a_\psi \frac{\partial^2 \psi}{\partial t^2} + e_\psi \frac{\partial \psi}{\partial t} = L_1(\psi), \quad a_R \frac{\partial^2 R}{\partial t^2} + e_R \frac{\partial R}{\partial t} = L_2(R), \tag{19}$$

via an explicit-in-time discretization with $t = n\Delta t$. The constants a_ψ and a_R are chosen to maintain numerical stability of the scheme with the time step Δt on the same order as the spatial mesh, and the coefficients e_ψ and e_R are chosen dynamically to optimize convergence [5]. In practice, the right hand sides of Eq. (19) are preconditioned to accelerate convergence, and the iteration is actually performed in Fourier space by updating the Fourier coefficients of R and ψ with respect to the angular coordinates [24].

An example of a numerical solution with a resonant flux surface computed using NSLAB is shown in Fig. 2, demonstrating that the slab geometry also supports singular behavior similar to that observed using NSTAB. The spacing of the flux surfaces reflects a resonance where $\iota(s) = 1$, and the surfaces display a corresponding symmetry with poloidal and toroidal mode numbers $(m, n) = (1, 1)$. Further examples will be discussed in more detail in Section 4. We first include a discussion of the singularities present in a linerarized treatment of small amplitude perturbations of a planar geometry.

3 Linearized Equations

To illustrate the resonances at rational flux surfaces, it is useful to consider the linearized governing equations for small-amplitude perturbations of two planar flux surfaces bounding the plasma. Specifically, we consider a perturbation expansion of the MHD equilibrium relative to a one-dimensional base state corresponding to flat walls $z_0 = a_0$ and $z_1 = b_0$. We consider a normal mode perturbation of the system with wavenumber (m, n), with a small expansion parameter ϵ, $|\epsilon| \ll 1$, which results in a linear problem at first order in ϵ. The expansion is performed with the aid of a computer algebra system; we omit the details and summarize the results.

The perturbed bottom and top walls are assumed to take the form

$$z_0(u, v) = a_0 + \epsilon a_{mn} \cos 2\pi(mu - nv), \quad z_1(u, v) = b_0 + \epsilon b_{mn} \cos 2\pi(mu - nv), \tag{20}$$

respectively, and their difference $z_2(u, v) = z_1(u, v) - z_0(u, v)$ is denoted by

$$z_2(u, v) = c_0 + \epsilon c_{mn} \cos 2\pi(mu - nv), \tag{21}$$

with $c_{mn} = b_{mn} - a_{mn}$. The corresponding expansion for $R(s,u,v)$ is

$$R(s,u,v) = R_0(s) + \epsilon R_{mn}(s)\, \cos 2\pi(mu - nv) + O(\epsilon^2), \tag{22}$$

and that for $\psi(s,u,v)$ is

$$\psi(s,u,v) = \pi[u - \iota(s)v] + \epsilon\psi_{mn}(s)\, \sin 2\pi(mu - nv) + O(\epsilon^2). \tag{23}$$

Note the presence of the sin function as opposed to the cos function for R for the normal mode representation of $\psi(s,u,v)$, which corresponds to the difference in the number of derivatives appearing for $\psi(s,u,v)$ and $R(s,u,v)$ in the governing equations.

3.1 Base State

Expanding in ϵ gives the leading order nonlinear ordinary differential equation for the one dimensional base state,

$$R_0''(s) - \left[\frac{L_x^2\, \iota(s)\, \iota'(s)}{(L_y^2 + [\iota(s)]^2\, L_x^2)}\right] R_0'(s) - \left[\frac{c_0^2 L_x^2\, L_y^2\, p'(s)}{\pi^2(L_y^2 + [\iota(s)]^2\, L_x^2)}\right] [R_0'(s)]^3 = 0, \tag{24}$$

with $R_0(0) = 0$ and $R_0(1) = 1$. The solution depends on the dimensions a_0, b_0, L_x and L_y of the system, the rotational transform $\iota(s)$, and the pressure gradient $p'(s)$. In the force-free case with $p'(s) = 0$, and with zero shear, $\iota'(s) = 0$, the solution is just $R_0(s) = s$. The general case requires the numerical solution of this nonlinear differential equation.

3.2 First Order Equations

At first order, we obtain a linear equation that can be solved for the perturbation $\psi_{mn}(s)$ in terms of c_{mn}/c_0 and $R_{mn}'(s)/R_0'(s)$,

$$\psi_{mn}(s) = \frac{[L_y^2 m + L_x^2 n\iota(s)]}{2[L_y^2 m^2 + L_x^2 n^2]} \left[\frac{c_{mn}}{c_0} + \frac{R_{mn}'(s)}{R_0'(s)}\right]. \tag{25}$$

The perturbation $R_{mn}(s)$ satisfies the linear second order ordinary differential equation

$$\alpha_1 R_{mn}''(s) + \alpha_2 R_{mn}'(s) + \alpha_3 R_{mn}(s) + \gamma = 0, \tag{26}$$

where the coefficients in these equations are

$$\alpha_1 = \frac{-L_x L_y \pi^2 [n - m\iota(s)]^2}{c_0 (L_y^2 m^2 + L_x^2 n^2)[R_0'(s)]^2}, \tag{27}$$

$$\alpha_2 = \frac{L_x L_y \pi^2 [L_x^2 (3n\iota(s) - m\iota(s)^2) + 2L_y^2 m]\,[n - m\iota(s)]\,\iota'(s)}{c_0 (L_y^2 m^2 + L_x^2 n^2)(L_y^2 + L_x^2 [\iota(s)]^2)[R_0'(s)]^2} \tag{28}$$

$$+ \frac{3 c_0 L_x^3 L_y^3 [n - m\iota(s)]^2 p'(s)}{(L_y^2 m^2 + L_x^2 n^2)(L_y^2 + L_x^2 [\iota(s)]^2)}$$

$$\alpha_3 = \frac{4 c_0 \pi^4 [n - m\iota(s)]^2)}{L_x L_y}, \tag{29}$$

and the inhomogeneous term is

$$\gamma = \frac{2 c_{mn} L_x^3 L_y^3\, R_0'(s)\,[n - m\iota(s)]^2\, p'(s)}{(L_y^2 m^2 + L_x^2 n^2)(L_y^2 + L_x^2 [\iota(s)]^2)} \tag{30}$$

$$+ \frac{2 c_{mn} L_x L_y \pi^2\,[L_y^2 m + L_x^2 n]\,[n - m\iota(s)]\,\iota(s)\,\iota'(s)}{c_0^2 (L_y^2 m^2 + L_x^2 n^2)(L_y^2 + L_x^2 [\iota(s)]^2) R_0'(s)}$$

$$+ \frac{4\pi^4\,[a_{mn} + c_{mn} R_0(s)]\,[n - m\iota(s)]^2}{L_x L_y}.$$

Note the common appearance of the resonant factor $[n - m\iota(s)]$ in each coefficient. In particular, the terms involve the factors $[n - m\iota(s)]\iota'(s)$ and $[n - m\iota(s)]^2 p'(s)$. For vanishing shear, $\iota'(s) = 0$, each remaining term contains a quadratic factor of $[n - m\iota(s)]^2$, and the singularity at $\iota(s) = n/m$ is removable. This result is in agreement with the well-known result that nonsymmetric equilibria with nested flux surfaces can be constructed for constant rotational transform [25, 22]. On the other hand, with moderate shear $\iota'(s_0) \neq 0$ at the resonant surface $s = s_0$, Eq. (26) is singular at s_0, and the leading order behavior of the singularity does not change qualitatively with changes in $p'(s_0)$. The case of small shear is thus a singular limit of Eq. (26), and finite pressure effects can be significant in this case.

3.3 Numerical Example

As an example, we take $L_x = L_y = 1$, $a_0 = a_{mn} = 0$, $b_0 = b_{mn} = 1$, and

$$\iota(s) = 0.25 + 0.5\,s, \quad p(s) = 1.5\,s(1 - s), \tag{31}$$

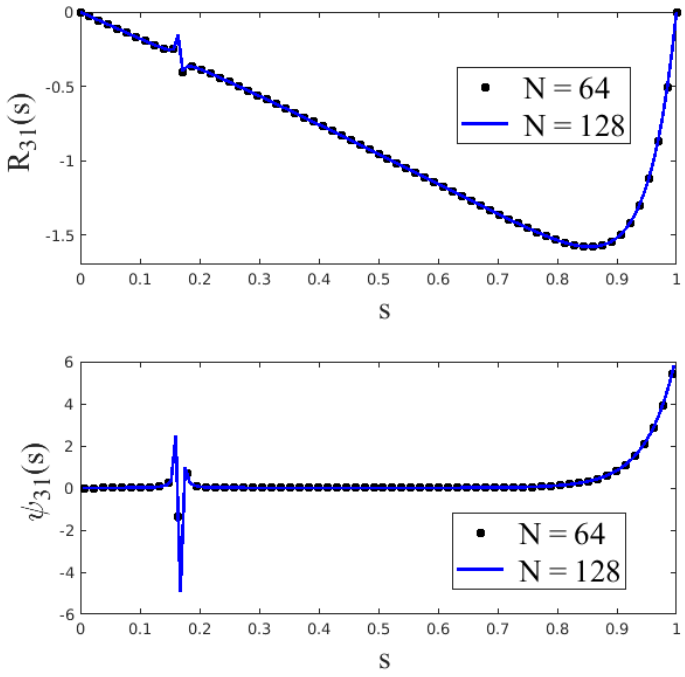

Figure 3: Numerical solution of Eqs. (25) and (26) for $R_{31}(s)$ and $\psi_{31}(s)$ for the parameters and profiles given in Section 3.3 using 64 grid points (black dots) and 128 grid points (blue curves). A singularity is present at the surface where $\iota(s) = 1/3$.

and we consider the resonant surface where $\iota(s) = 1/3$ by adding a $(3, 1)$ harmonic to the external boundary. A finite difference solution for $R_{31}(s)$, and the corresponding solution $\psi_{31}(s)$, is shown in Figure 3. We do not attempt any special treatment of the singularity in this simple case, since this is consistent with the specific finite difference scheme employed in NSTAB and NSLAB, and the solution in Fig. 3 should therefore reproduce the behavior expected in those codes for small amplitude perturbations. In this case, the resonant surface where $\iota(s) = 1/3$ at $s \approx 0.167$ does not lie on the numerical grid, and the solution is exhibiting singular behavior at nearby mesh points. Note that there are continuous gradients in $R_{31}(s)$ (and in $\psi_{31}(s)$, which is coupled to $R'_{31}(s)$) near the walls where $R_{31}(s)$ vanishes, although these smooth variations are easily distinguished

from the singular behavior at the resonant surface.

4 NSLAB Numerical results

We start the discussion of the NSLAB numerical results with a comparison of the linearized results from the previous section with a corresponding nonlinear NSLAB computation for a small-amplitude, single-mode perturbation of the upper wall. Our examples will all feature a flat lower surface, $z_0(u, v) = 0$, with $L_x = L_y = 1$.

4.1 Comparison of NSLAB and Linearized Results

We consider a force-free case with $p'(s) = 0$ and rotational transform $\iota(s) = 0.95 + 0.1s$, focusing on a $(1, 1)$ mode at the resonant surface $s_0 = 1/2$. The upper surface is given

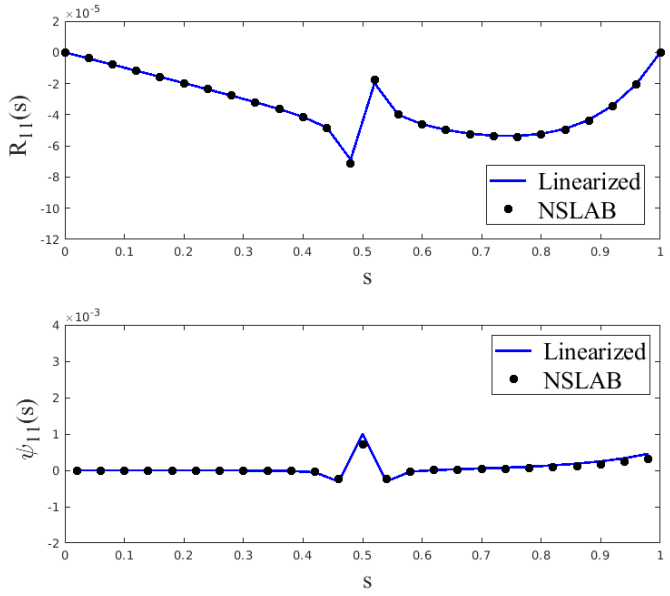

Figure 4: Comparison between the linearized solution (blue curve) and the corresponding NSLAB computation (black dots) for the slab equilibrium described in Section 4.1.

by

$$z_1(u,v) = 1 + \Delta_{11}\cos 2\pi(u-v), \tag{32}$$

with amplitude $\Delta_{11} = 10^{-4}$. The comparison is illustrated in Fig. 4, where we show ψ_{11} given by the analytic linear calculation and the $(1,1)$ Fourier harmonic of NSLAB's nonlinear solution for $\psi(s,u,v)$. On a mesh of 25 points, the agreement is seen to be quite satisfactory. The numerical solution for $\psi_{11}(s)$ shows a localized peak at the three mesh points centered at $s_0 = 1/2$. As a rough indicator of the strength of the singularity, we use

$$D^2\psi_{11} = \frac{\psi_{11}(s_0) - [\psi_{11}(s_0+h) + \psi_{11}(s_0-h)]/2]}{h^2} \approx \frac{1}{2}\frac{d^2\psi_{11}}{ds^2}(s_0) \tag{33}$$

where h is the mesh spacing in s. As well as approximating $\psi''_{11}(s_0)/2$, $D^2\psi_{11}$ characterizes the peak amplitude relative to the average value of the two neighboring values. Since $\mathbf{J} = \nabla\times[\nabla\times(\psi\nabla s)]$, $\psi''_{11}(s_0)$ is an effective measure of the singular current strength. For the case shown in Fig. 4, we find $D^2\psi_{11} = 0.5938$. At this point, we stress that we recognize that the computation of equilibria with a localized singularity on a fixed mesh is necessarily plagued by relatively high levels of truncation error. However, we will not be concerned by this numerical issue since our goal for the remainder of the article is to find appropriate wall shapes that, as much as possible, eliminate these singularities. The resulting smooth solution can then achieve the level of accuracy that is expected of a second-order-accurate finite difference scheme.

4.2 Eliminating Current Sheets by Wall Modification

The remainder of the article focuses on our central motivation for this work, namely the elimination current sheets by suitable modifications of the shape of the upper wall. We consider various cases with one, two, and three resonant surfaces for force-free equilibria with $p'(s) = 0$ or for finite pressure equilibria with $p(s) = p_0(1-s^2)^2$. In this study, we consider relatively weak current sheets that can be eliminated by small amplitude perturbations of a flat upper wall. We generally represent the upper wall as a finite

Fourier series

$$z_1(u,v) = \sum_{m,n} \Delta_{mn} \cos 2\pi(mu - nv) \tag{34}$$

where the mean position of the wall is $\Delta_{00} = 1$. The magnitude of the pressure in the finite-pressure equilibria we will study will be expressed in terms of the usual β parameter, defined by

$$\beta = \frac{2\int_V p\, dV}{\int_V |\mathbf{B}|^2 dV}, \tag{35}$$

and which can be determined from a numerical integration once the solution has been computed.

4.2.1 Single Resonant Surface

For the case of a single resonant surface, we consider the rotational transform profile $\iota(s) = 0.35 + 0.3s$. To generate a (2,1) current sheet, we start with a perturbed upper wall with $(2,0)$ and $(0,1)$ harmonics,

$$z_1(u,v) = 1 + 0.01\cos 4\pi u + 0.01\cos 2\pi v. \tag{36}$$

The nonlinear interaction of the $(2,0)$ and $(0,1)$ modes is found to generate at quadratic order a $(2,1)$ mode that triggers a current sheet at the resonant surface $s_0 = 1/2$, where $\iota(s_0) = 1/2$.

Some numerical results are given in Fig. 5 for a case with $p_0 = 0.3$ corresponding to $\beta = 2.5\%$. The top two plots in the figure show the $(2,1)$ Fourier components $R_{21}(s)$ and $\psi_{21}(s)$ of the computed solutions $R(s,u,v)$ and $\psi(s,u,v)$. It is also insightful to consider the profiles for two other quantities which have an immediate physical interpretation, namely the parallel current density and the Jacobian of the coordinate transformation, which can be viewed as a measure of the distortion of the flux surfaces associated with the appearance of a current sheet. The $(2,1)$ Fourier component of the parallel current, $Jp_{21}(s)$ of $Jp(s,u,v)$ in (17), and the $(2,1)$ Fourier component of the Jacobian $J(s,u,v)$ in (8), $JD_{21}(s)$, are shown as the bottom two plots in Fig. 5. Both the parallel current and the Jacobian profiles show singular behavior that is qualitatively similar to $\psi_{21}(s)$,

with peaked singularities that are localized near $s = s_0$. In our computations, we generally find that the behavior of the parallel current profiles $Jp_{mn}(s)$ is faithfully mirrored by that of the $\psi_{mn}(s)$ profiles. We emphasize that all four quantities plotted in Fig. 5 exhibit related singular behavior at the resonant flux surface. In particular, this figure illustrates the finding that the spacing of the flux surfaces near the resonance, as determined by the mapping Jacobian $JD_{21}(s)$, is related to the current sheet singularity, albeit via a numerical computation. Indeed, we will see below that a strategy to eliminate the singularity in just one of the four quantities also simultaneously eliminates the singularities in the other three as well.

On the left-hand side of Fig. 6, we show the parallel current profile in the vicinity of the resonant surface $s = s_0$ for a series of mesh refinements using $ns = 25$, 49, 65, and 97 mesh points for the s coordinate. With decreasing mesh size $1/ns$ the peak increases in magnitude, while the width of the peak decreases. The figure on the right-hand side of Fig. 6 shows a scaled version of the figure on the left-hand side of Fig. 6, where the vertical axis is scaled by ns^2 and the horizontal axis by $1/ns$. We observe that a satisfactory calculation of the singularity is captured using a relatively crude mesh. This can be attributed to the use of a carefully designed conservative difference scheme in NSLAB (following that used in NSTAB), which avoids smearing the singularity over too many neighboring mesh points.

We next consider the feasibility of eliminating the singularity at the $s_0 = 1/2$ surface by varying the fundamental harmonic Δ_{21} of the wall perturbation. We consider $p_0 = 0.68$, corresponding to a high-beta equilibrium with $\beta = 5.8\%$. The profile for the $(2, 1)$ Fourier component $\psi_{21}(s)$ of $\psi(s, u, v)$ for $\Delta_{21} = 0$ is shown in the top three figures in Fig. 7. The quadratic interaction of the $(2, 0)$ and $(0, 1)$ wall perturbations has generated a small-amplitude current sheet with a negative value of $\psi_{21}(s_0)$. The corresponding value of $D^2\psi_{21}$ in Eq. (33) is $D^2\psi_{21} = -1.076$. We note that, as one would expect, $D^2\psi_{21}$ scales quadratically in the magnitude of the wall perturbation amplitude, as can be verified by reducing the magnitude of the wall perturbations by half so that $\Delta_{20} = \Delta_{01} = 0.005$,

which results in an observed four-fold decrease in $D^2\psi_{21}$ to $D^2\psi_{21} = -0.269$.)

If we then explicitly introduce a (2,1) wall perturbation of amplitude Δ_{21}, so that

$$z_1(u,v) = 1 + 0.01\cos 4\pi u + 0.01\cos 2\pi v + \Delta_{21}\cos 2\pi(2u - v) \tag{37}$$

we find that the peak in $\psi_{21}(s_0)$ monotonically increases from negative values, through zero, and then on to positive values as Δ_{21} is increased from zero through positive values. For example, the third plot in Fig. 7 for $\Delta_{21} = 0.003$ shows a positive peak in $\psi_{21}(s_0)$, with $D^2\psi_{21} = 1.301$. At the intermediate value $\Delta_{21} = 0.001359$, we find that $D^2\psi_{21}$ passes through zero, and the second figure in Fig. 7 corresponding to that case shows a smooth profile for $\psi_{21}(s)$ in the vicinity of the resonant surface: the singularity has been removed. In the bottom three plots in Fig. 7, we show the corresponding plots for the $(2,1)$ Fourier component $R_{21}(s)$ of the other dependent variable $R(s,u,v)$, which also exhibits singular behavior at s_0 that is similarly eliminated by modifying the shape of the upper wall.

The critical value of the $(2,1)$ wall perturbation Δ_{21} that eliminates the current sheet with $D^2\psi_{21} = 0$ can be computed by performing a series of NSLAB runs, effectively conducting a root-finding search by considering $D^2\psi_{21}$ to be a function of Δ_{21}. More efficiently, this search can instead be incorporated into the overall NSLAB iterative procedure in Eq. (19) by appending an additional evolution equation

$$a_{21}\frac{d\Delta_{21}}{dt} = -D^2\psi_{21} \tag{38}$$

where a_{21} is a positive relaxation coefficient. In this way, the critical value of the wall perturbation Δ_{21} that drives the singularity amplitude $D^2\psi_{21}$ to zero as the iteration converges can be found in a single NSLAB run. We numerically observe that just like $D^2\psi_{21}$, this critical value of Δ_{21} scales quadratically with the amplitude of the wall perturbation we imposed to generate the current sheet. Furthermore, for the small perturbations considered in this work, we empirically observed that $D^2\psi_{21}$ depended linearly on Δ_{21}, with a slope somewhat steeper for the finite pressure gradient case discussed here as compared to the zero pressure gradient case discussed next. In that sense, we may say that the

elimination of the current sheet is robust to small changes in the amplitude of the applied resonant component.

In Fig. 8, we again consider the rotational transform profile $\iota(s) = 0.35 + 0.3s$, for a force-free equilibrium $p'(s) = 0$. In this case, we find an optimal value of $\Delta_{21} = 0.001604$ that results in $D^2\psi_{21} \approx 0$. Comparing with the corresponding profiles in Fig. 7, we find that decreasing β to zero amplitude has reduced the peaks in ψ_{21} by roughly half; the same is true for the corresponding values of $D^2\psi_{21}$. We generally find that the sensitivity of the amplitude of the computed current sheets to β is increased as the shear $\iota'(s)$ decreases. For larger shear, the results tend to become insensitive to β; this is consistent with the findings for the linear analysis of normal modes described in the previous section.

4.2.2 Two Resonant Surfaces

We next consider the rotational transform profile $\iota(s) = 0.4 + 0.4s$, which includes the low-order rationals $\iota = 1/2$ and $\iota = 2/3$, and we trigger singularities by prescribing the fixed wall perturbations with $(2, 0)$ and $(0, 1)$ components to generate a $(2, 1)$ mode via nonlinear coupling, and wall perturbations with $(3, 0)$ and $(0, 2)$ components to generate a $(3, 2)$ mode, so that we have two prominent resonant surfaces at $s_{21} = 1/4$, and $s_{32} = 2/3$. for $\iota(s_{21}) = 1/2$ and $\iota(s_{32}) = 2/3$. Specifically, the upper surface is

$$z_1(u, v) = 1 + 0.01\cos 4\pi u + 0.01\cos 2\pi v + \Delta_{21}\cos 2\pi(2u - v) \tag{39}$$
$$+ 0.01\cos 6\pi u + 0.01\cos 4\pi v + \Delta_{32}\cos 2\pi(3u - 2v).$$

The resulting equilibrium with pressure profile $p(s) = 0.75(1 - s^2)^2$, corresponding to $\beta = 5.8\%$, and $\Delta_{21} = \Delta_{32} = 0$ is shown in Fig. 9. The profiles for $\psi_{21}(s)$ and $\psi_{32}(s)$ are plotted on similar scales but with an inset for $\psi_{21}(s)$ to better show the $(2, 1)$ singularity around s_{21}. To eliminate the singularities, we generalize the iteration in Eq. (38) to

$$a_{21}\frac{d\Delta_{21}}{dt} = -D^2\psi_{21}, \quad a_{32}\frac{d\Delta_{32}}{dt} = -D^2\psi_{32}, \tag{40}$$

where $D^2\psi_{21}$ and $D^2\psi_{32}$ are based at s_{21} and s_{32}, respectively. The iteration produces critical wall perturbation values $\Delta_{21} = 0.001147$ and $\Delta_{32} = 0.001998$ that eliminate

the singularities as shown in Fig. 10. We mention here that to compute the critical wall perturbation values Δ_{21} and Δ_{32}, we have also used a quasi-Newton method in a separate run, described in section 4.2.3, and obtained the same results. We note that the same scales are used in the plots of Fig. 9 and Fig. 10. We again observe that the Fourier harmonics ψ_{21} and ψ_{32} of ψ, and Jp_{21} and Jp_{32} of Jp have the same behavior, and that we indeed eliminated the current singularity.

4.2.3 Three Resonant Surfaces

Our final case is to consider three resonant surfaces, with a rotational transform $\iota(s) = 0.4+0.5s$ admitting the low-order rationals 1/2, 2/3, and 3/4. For the force-free $p'(s) = 0$ case shown in Fig. 11, we set the boundary coefficients $\Delta_{20} = \Delta_{30} = \Delta_{40} = \Delta_{01} = \Delta_{02} = \Delta_{03} = 0.01$. There are singularities of ψ_{21}, ψ_{32} and ψ_{43} around the flux surfaces $s_{21} = 1/5$, $s_{32} = 8/15$ and $s_{43} = 7/10$, respectively. In this case, the generalization of Eq. (40) to the computation with three resonant surfaces is very slow to converge, and we have employed an alternate strategy. We observe that a change of one wall harmonic, say Δ_{21}, can have a significant effect on all three singularities $D^2\psi_{21}$, $D^2\psi_{32}$, and $D^2\psi_{43}$, so that the straightforward procedure that drives each wall harmonic by its corresponding singular mode in Eq. (38) or Eq. (40) can become ineffective. We therefore iterate on the coefficients by coupling their influence though a simple version of a quasi-Newton procedure, setting

$$\begin{pmatrix} \Delta_{21}^{(n+1)} \\ \Delta_{32}^{(n+1)} \\ \Delta_{43}^{(n+1)} \end{pmatrix} = \begin{pmatrix} \Delta_{21}^{(n)} \\ \Delta_{32}^{(n)} \\ \Delta_{43}^{(n)} \end{pmatrix} - F^{-1} \begin{pmatrix} D^2\psi_{21}^{(n)} \\ D^2\psi_{32}^{(n)} \\ D^2\psi_{43}^{(n)} \end{pmatrix}, \tag{41}$$

where F is the 3×3 Jacobian $\partial(D^2\psi_{21}, D^2\psi_{32}, D^2\psi_{43})/\partial(\Delta_{21}, \Delta_{32}, \Delta_{43})$ computed approximately via finite differences from separate NSLAB runs with varying wall perturbations. Eq. (41) can also be regarded as the discretized form of a first order ordinary differential equation in time that couples the dependence on the three wall harmonics. This procedure produces good values for the critical wall harmonics with only a few NSLAB runs,

and we find the critical values $\Delta_{21} = 0.00083$, $\Delta_{32} = 0.00222$, and $\Delta_{43} = 0.00192$ as shown in Fig. 12. We again observe that the behaviors of the parallel current Jp_{21} and ψ_{21}, Jp_{32} and ψ_{32}, and Jp_{43} and ψ_{43} are qualitatively similar.

5 Discussion

We have developed a modified version of the MHD equilibrium and stability code NSTAB [24] in a slab geometry that avoids complications arising from the magnetic axis in toroidal geometries. We have used this code to study the possibility of using suitable wall modifications to avoid the occurrence of singular current sheets that tend to arise at resonant flux surfaces where the rotational transform assumes low-order rational values [6, 7, 21, 23]. We find that a simple iterative procedure can be used to eliminate one or two current sheets, while a more complicated procedure that takes additional mode coupling into effect suffices to remove three sheets. We have restricted our attention to relatively weak current sheets that are generated by nonlinear interactions between "sideband" wall harmonics that can resonate with the fundamental harmonics associated with the resonant flux surfaces. We have considered both force-free examples and examples with finite pressure gradients. Remarkably, finite pressure gradients at the resonant surfaces do not prevent us from removing the singularities at these surfaces, and do not affect the behavior of our solver. This could be an artifact of our focus on small wall perturbations and slab equilibria, although preliminary results in a toroidal geometry with the NSTAB code suggest otherwise, as we have found that we are also able to remove small-amplitude current singularities in some NSTAB toroidal equilibria with finite pressure gradients. We are currently investigating this question from a slightly broader viewpoint; namely, we want to determine whether there exist current singularities which cannot be removed by suitable boundary perturbations.

We have emphasized the role played by a conservative difference scheme in capturing the singular current sheets over a width of one or two mesh points. A complementary

approach is to expressly add in smoothing terms that smear out such singularities over several mesh points to improve the robustness of the computation. This might be termed an "artificial resistivity" approach that resembles the "artificial viscosity" schemes that are used successfully in computational fluids dynamics to capture shocks (see, e.g., [11]). Also in this spirit an analysis of such smoothing effects on parallel current singularities at a resonant surface has been given by Hudson [18], with suggested applications to equilibrium calculations. We also note that the conservative difference scheme used in NSTAB and NSLAB, while often able to resolve moderate singularities compactly, can also lead to mesh-dependent non-convergence of the scheme if the Jacobian J of the mapping becomes very large or very small near a resonant surface.

A related topic to our treatment of the removal of current sheet singularities by appropriate wall perturbations is the topological changes made possible by the inclusion of resistive effects that can lead to the breaking and reconnection of field lines [13, 17]. These effects are generally dynamic and dissipative in nature, in contrast to the flux-conserving equations of ideal magnetohydrodynamics that underlie our treatment of static equilibria that minimize the magnetic energy over a class of solenoidal fields with nested flux surfaces. In both cases, these complementary models address the possibility of regularizing current sheet singularities, albeit via quite distinct processes.

It would be worthwhile to do a direct comparison of our measure of the singular current amplitude, $D^2\psi_{mn}$, in a nested flux surface model, with an island width computed without the assumption of nest flux surfaces; for example, one computed by using field line tracing with a force-free code. Measures of island width inferred from nested flux surface computations have been discussed previously (see, e.g., [6, 7]), but these arguments ultimately amount to conjectured scaling relations in the absence of a direct comparison. This is also an important subject for future research.

Acknowledgements

The authors thank H. Weitzner for suggesting this problem to us, and are grateful for many insightful discussions with D. Josell, W. Sengupta, and H. Weitzner. The research of EK and AJC was partially supported by the U.S. Department of Energy, Office of Science, Fusion Energy Sciences under Awards No. DE-FG02-86ER53223 and DE-SC0012398, and the Simons Foundation/SFARI (560651, AB).

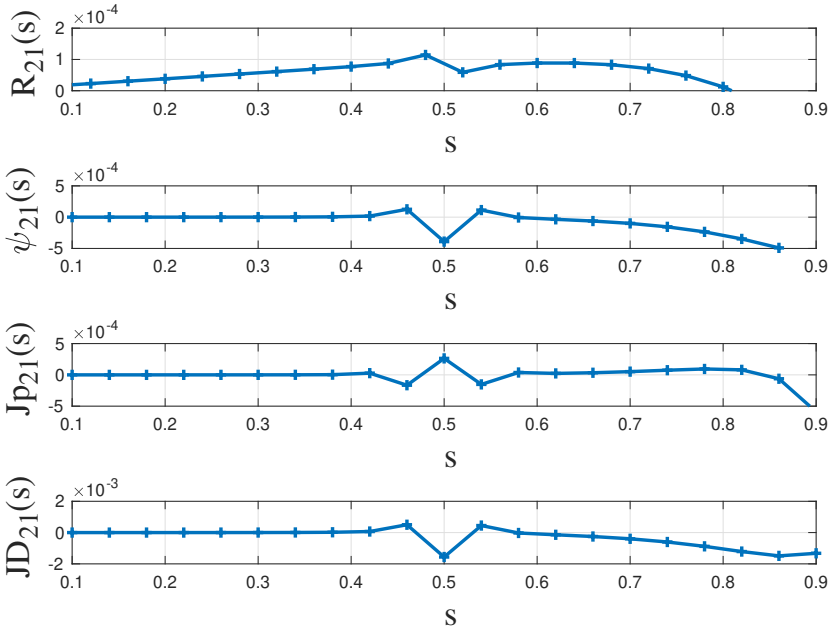

Figure 5: Slab equilibrium with a single resonant surface with singularity at $s_0 = 1/2$. The rotational transform profile is $\iota(s) = 0.35 + 0.3s$, the pressure profile is $p(s) = 0.3(1 - s^2)^2$, $\beta = 2.5\%$, and the wall perturbations correspond to $\Delta_{20} = \Delta_{01} = 0.01$ and $\Delta_{21} = 0$. From top to bottom, we plot the (2,1) Fourier component $R_{21}(s)$ of $R(s, u, v)$, the (2,1) Fourier component $\psi_{21}(s)$ of $\psi(s, u, v)$, the (2,1) Fourier component $Jp_{21}(s)$ of the parallel current $Jp(s, u, v)$, and the (2,1) Fourier component $JD_{21}(s)$ of the Jacobian $J(s, u, v)$, all as a function of flux surface coordinate s.

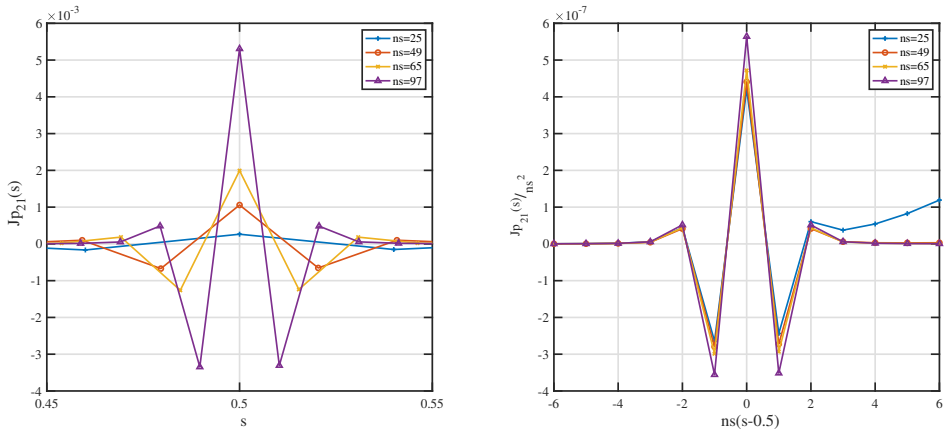

Figure 6: Single resonant surface with singularity at $s_0 = 1/2$: the rotational transform $\iota(s) = 0.35 + 0.3s$ and the pressure field $p(s) = 0.3(1-s^2)^2$, with $\beta = 2.5\%$. The Fourier component $Jp_{21}(s)$ of the parallel current $Jp(s,u,v)$ (see (17)), as a function of flux surface s with the wall perturbations $\Delta_{20} = \Delta_{01} = 0.01$ and $\Delta_{21} = 0$. The parallel current profiles $Jp_{21}(s)$ near $s = 0.5$ for the mesh refinements using $ns = 25$, 49, 65, and 97 points in the s coordinates (left) and their scaled versions (right).

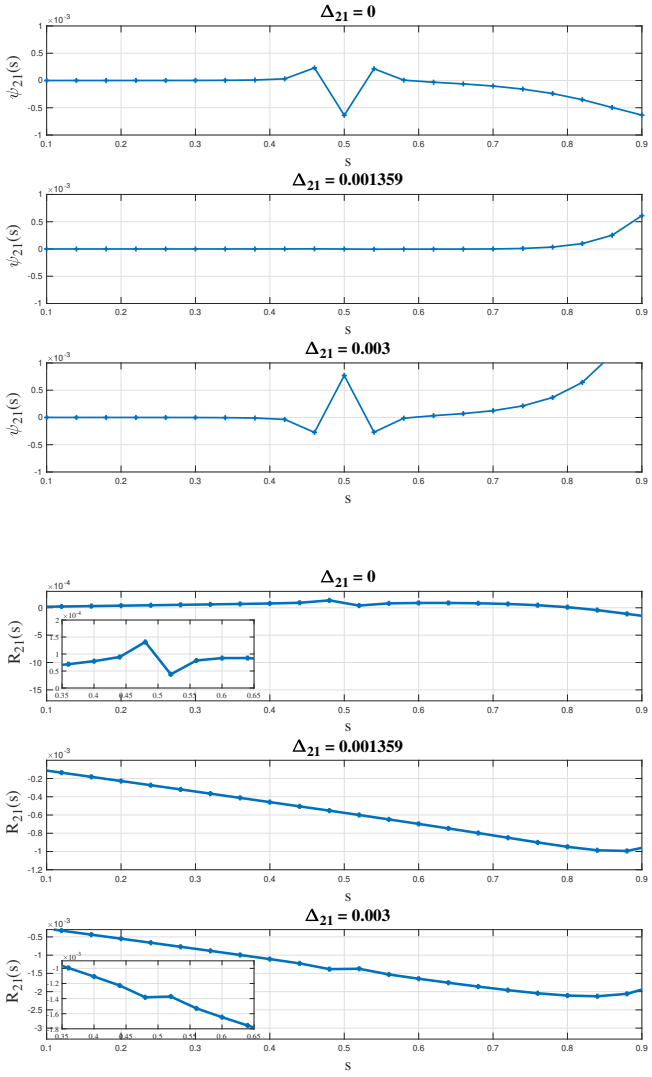

Figure 7: Single resonant surface with singularity at $s_0 = 1/2$ with finite pressure gradients. The rotational transform profile is $\iota(s) = 0.35 + 0.3s$, the pressure profile is $p(s) = 0.68(1 - s^2)^2$, $\beta = 5.8\%$, and the wall perturbation amplitudes are $\Delta_{20} = \Delta_{01} = 0.01$, and three different amplitudes for Δ_{21}. From top to bottom, we plot the Fourier component $\psi_{21}(s)$ of $\psi(s, u, v)$ with $\Delta_{21} = 0$, $\Delta_{21} = 0.001359$, and $\Delta_{21} = 0.003$ and the Fourier component $R_{21}(s)$ of $R(s, u, v)$ with $\Delta_{21} = 0$, $\Delta_{21} = 0.001359$, and $\Delta_{21} = 0.003$, all as a function of the flux coordinate s.

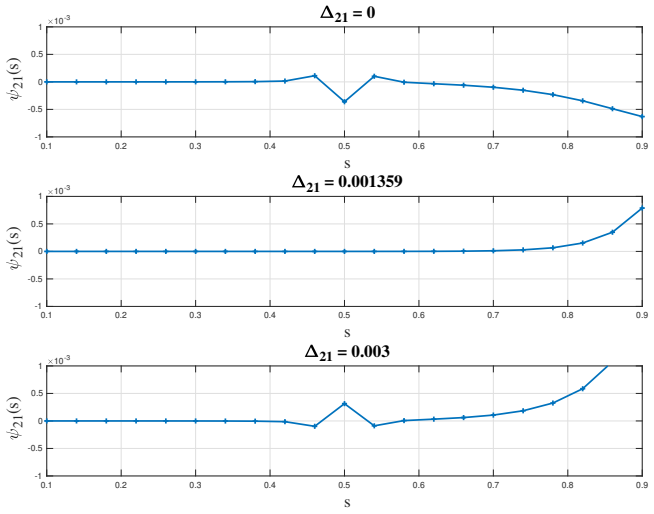

Figure 8: Single resonant surface with singularity at $s_0 = 1/2$ for force-free field. The Fourier component $\psi_{21}(s)$ of $\psi(s, u, v)$ as a function of the flux coordinate s for force-free equilibria with rotational transform profile $\iota(s) = 0.35 + 0.3s$, wall perturbation amplitudes $\Delta_{20} = \Delta_{01} = 0.01$, and three different amplitudes for Δ_{21}: $\Delta_{21} = 0$ (top), $\Delta_{21} = 0.001604$ (middle), and $\Delta_{21} = 0.003$ (bottom).

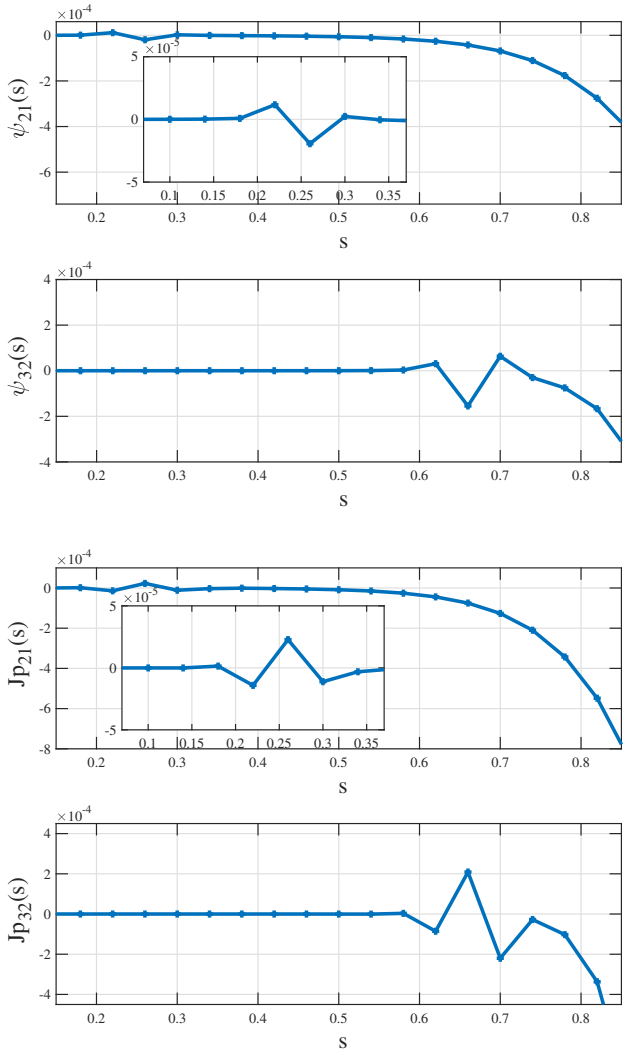

Figure 9: Two resonant surfaces with singularities at $s_{21} = 1/4$, and $s_{32} = 2/3$. The rotational transform profile is $\iota(s) = 0.4 + 0.4s$, the pressure profile is $p(s) = 0.75(1 - s^2)^2$, $\beta = 5.8\%$, and the wall perturbation amplitudes are $\Delta_{20} = \Delta_{30} = \Delta_{01} = \Delta_{02} = 0.01$ and $\Delta_{21} = \Delta_{32} = 0$. From top to bottom, we plot the (2,1) Fourier component $\psi_{21}(s)$ and the (3,2) Fourier component $\psi_{32}(s)$ of $\psi(s, u, v)$, the (2,1) Fourier component $\mathrm{Jp}_{21}(s)$, and the (3,2) Fourier component $\mathrm{Jp}_{32}(s)$ of $\mathrm{Jp}(s, u, v)$, all as a function of the flux coordinate s for a slab equilibrium.

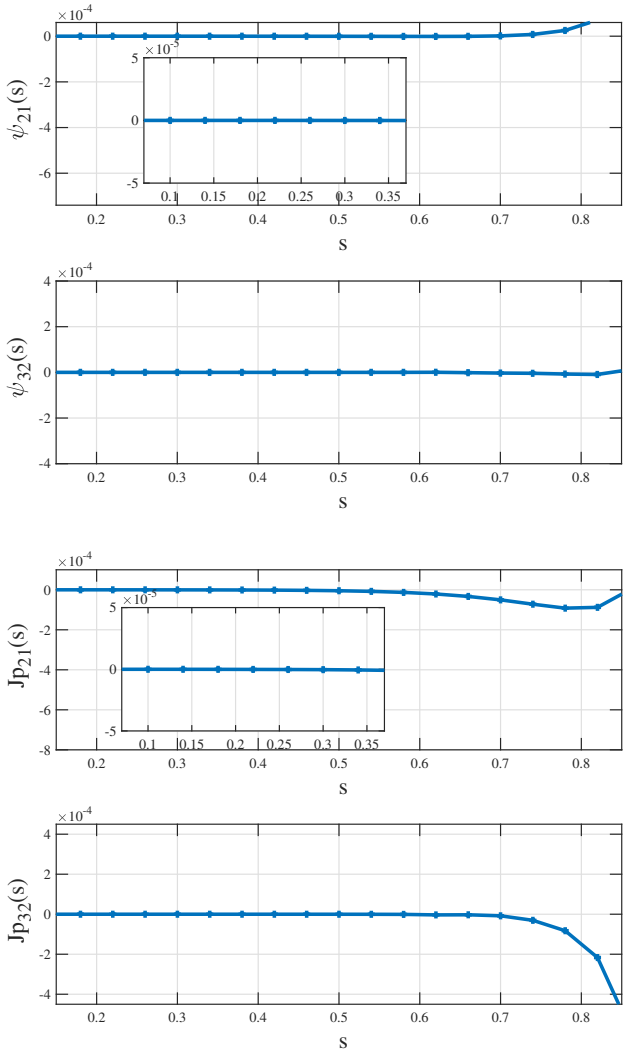

Figure 10: Two resonant surfaces with singularities at $s_{21} = 1/4$, and $s_{32} = 2/3$ removed. The rotational transform profile is $\iota(s) = 0.4 + 0.4s$, the pressure profile is $p(s) = 0.75(1 - s^2)^2$, $\beta = 5.8\%$, and the wall perturbation amplitudes are $\Delta_{20} = \Delta_{30} = \Delta_{01} = \Delta_{02} = 0.01$, $\Delta_{21} = 0.001147$, and $\Delta_{32} = 0.001998$. From top to bottom, we plot the (2,1) Fourier component $\psi_{21}(s)$, the (3,2) Fourier component $\psi_{32}(s)$ of $\psi(s, u, v)$, the (2,1) Fourier component $\mathrm{Jp}_{21}(s)$ and the (3,2) Fourier component $\mathrm{Jp}_{32}(s)$ of $\mathrm{Jp}(s, u, v)$, all as a function of the flux coordinate s for a slab equilibrium. Comparing these figures with figure 9, we observe that the singularity has been eliminated.

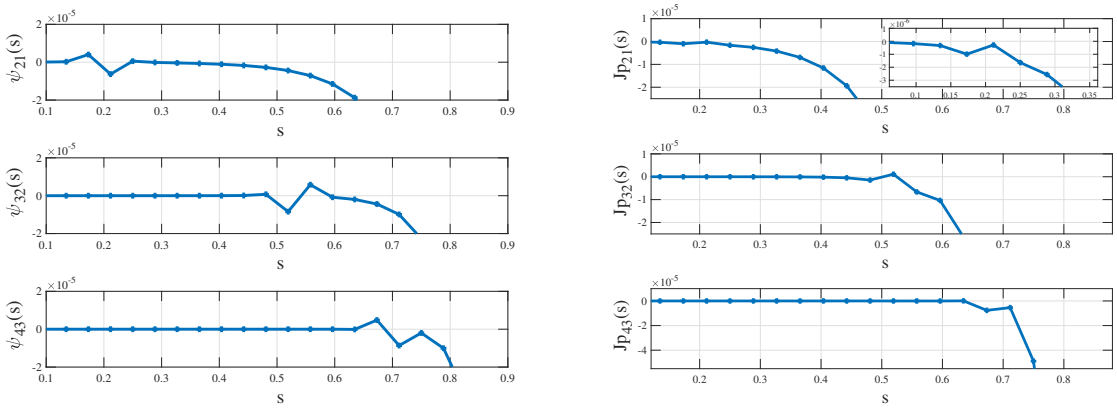

Figure 11: Three resonant surfaces with singularities at $s_{21} = 1/5$, $s_{32} = 8/15$ and $s_{43} = 7/10$. The rotational transform profile is $\iota(s) = 0.4 + 0.5s$, and the wall perturbation amplitudes are $\Delta_{20} = \Delta_{30} = \Delta_{40} = \Delta_{01} = \Delta_{02} = \Delta_{03} = 0.01$ and $\Delta_{21} = \Delta_{32} = \Delta_{43} = 0$. On the left, we plot the (2,1) Fourier component $\psi_{21}(s)$ (top), the (3,2) Fourier component $\psi_{32}(s)$ (middle), and the (4,3) Fourier component $\psi_{43}(s)$ (bottom) of $\psi(s, u, v)$, and on the right, we plot the (2,1) Fourier component $Jp_{21}(s)$ (top), the (3,2) Fourier component $Jp_{32}(s)$ (middle), and the (4,3) Fourier component $Jp_{43}(s)$ of $Jp(s, u, v)$ (bottom), all as a function of the flux coordinate s for a force-free slab equilibrium.

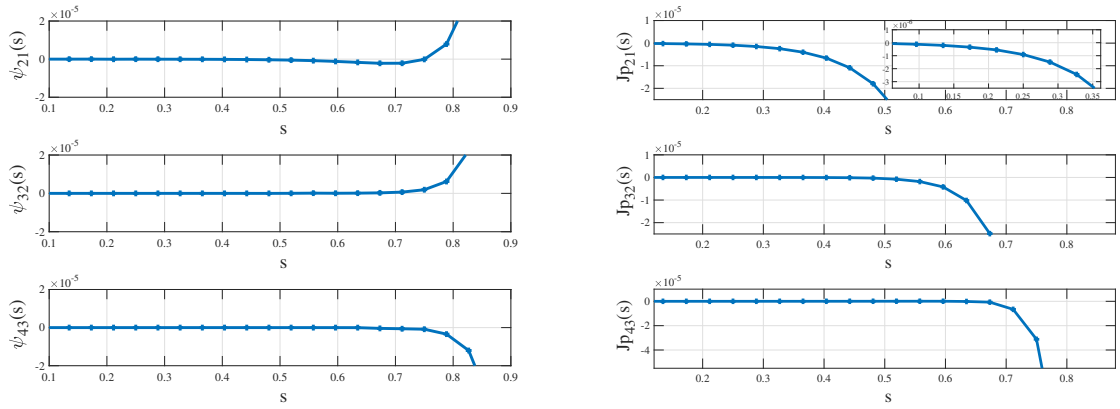

Figure 12: Three resonant surfaces with singularities at $s_{21} = 1/5$, $s_{32} = 8/15$ and $s_{43} = 7/10$ removed. The rotational transform profile is $\iota(s) = 0.4 + 0.5s$, and the wall perturbation amplitudes are $\Delta_{20} = \Delta_{30} = \Delta_{40} = \Delta_{01} = \Delta_{02} = \Delta_{03} = 0.01$, $\Delta_{21} = 0.00083$, $\Delta_{32} = 0.00222$, and $\Delta_{43} = 0.00192$. On the left, we plot the (2,1) Fourier component $\psi_{21}(s)$ (top), the (3,2) Fourier component $\psi_{32}(s)$ (middle), and the (4,3) Fourier component $\psi_{43}(s)$ (bottom) of $\psi(s, u, v)$, and on the right, we plot the (2,1) Fourier component $Jp_{21}(s)$ (top), the (3,2) Fourier component $Jp_{32}(s)$ (middle), and the (4,3) Fourier component $Jp_{43}(s)$ (bottom) of $Jp(s, u, v)$, all as a function of the flux coordinate s for a force-free slab equilibrium. Comparing these figures with Figure 11, we see that this particular choice of Δ_{21}, Δ_{32}, and Δ_{43} allowed us to eliminate the singularities at the resonant surfaces.

References

[1] G. Bateman. *MHD Instabilities*. MIT Press, Cambridge, MA, 1978.

[2] F. Bauer, O. Betancourt, and P. Garabedian. *A Computational Method in Plasma Physics*. Springer-Verlag, New York, 1978.

[3] F. Bauer, O. Betancourt, and P. Garabedian. *Magnetohydrodynamic Equilibrium and Stability of Stellarators*. Springer-Verlag, New York, 1984.

[4] F. Bauer, O. Betancourt, P. Garabedian, and M. Wakatani. *The Beta Equilibrium, Stability and Transport Codes*. Academic, Boston, 1987.

[5] O. Betancourt. BETAS, a spectral code for three-dimensional magnetohydrodynamic equilibrium and nonlinear stability calculations. *Communications on Pure and Applied Mathematics*, 41(5):551–568, 1988.

[6] O. Betancourt and P. Garabedian. Numerical analysis of equilibria with islands in magnetohydrodynamics. *Communications on Pure and Applied Mathematics*, 35, 1982.

[7] O. Betancourt and G. McFadden. Nonparametric solutions to the variational principle of ideal magnetohydrodynamics. *Lecture Notes in Pure and Applied Mathematics.*, 96:159–171, 1985.

[8] N. N. Bogoljubov, J. A. Mitropoliskij, and A. M. Samoilenko. *Methods of Accelerated Convergence in Nonlinear Mechanics*. Springer, Berlin, 2011.

[9] J. R. Cary. Vacuum magnetic fields with dense flux surfaces. *Physical Review Letters*, 49(4):276, 1982.

[10] J. R. Cary and J. D. Hanson. Stochasticity reduction. *The Physics of Fluids*, 29(8):2464–2473, 1986.

[11] P. Garabedian and G. McFadden. Design of the demo fusion reactor following iter. *Journal of Research of the National Institute of Standards and Technology*, 114:229–236, 2009.

[12] H. Grad. Some new variational properties of hydromagnetic equilibria. *Physics of Fluids*, 7(8):1283–1292, 1964.

[13] T. Hahm and R. Kulsrud. Forced magnetic reconnection. *Physics of Fluids*, 28(8):2412–2418, 1985.

[14] P. Helander. Theory of plasma confinement in non-axisymmetric magnetic fields. *Reports on Progress in Physics*, 77(8):087001, 2014.

[15] P. Helendar. Theory of plasma confinement in non-axisymmetric magnetic fields. *Reports on Progress in Physics*, 81, 2018.

[16] P. Hirshman and J. Whitson. Steepest-descent moment method for three-dimensional magnetohydrodynamic equilibria. *Physics of Fluids*, 26:3553S, 1983.

[17] P. Hu. Fast reconnection of magnetic fields in a plasma. *Physics of Fluids*, 26:2234–2239, 1983.

[18] S. Hudson. A regularized approach for solving magnetic differential equations and a revised iterative equilibrium algorithm. *Physics of Plasmas*, 17:114501, 2010.

[19] S. R. Hudson, D. Monticello, A. Reiman, A. Boozer, D. Strickler, S. Hirshman, and M. Zarnstorff. Eliminating islands in high-pressure free-boundary stellarator magnetohydrodynamic equilibrium solutions. *Physical Review Letters*, 89(27):275003, 2002.

[20] M. Kruskal and R. Kulsrud. Equilibrium of a magnetically confined plasma in a toroid. *Physics of Fluids*, 1:265, 1958.

[21] J. Loizu, S. Hudson, A. Bhattacharjee, and P. Helander. Magnetic islands and singular currents at rational surfaces in three-dimensional magnetohydrodynamic equilibria. *Physics of Plasmas*, 22(2):022501, 2015.

[22] D. Lortz. Über die existenz toroidaler magnetohydrostatischer gleichgewichte ohne rotationstransformation. *Zeitschrift für angewandte Mathematik und Physik ZAMP*, 21(2):196–211, Mar 1970.

[23] M. Mikhailov, J. Nührenberg, and R. Zille. Elimination of current sheets at resonances in three-dimensional toroidal ideal-magnetohydrodynamic equilibria. *Nuclear Fusion*, 59(6):066002, 2019.

[24] M. Taylor. A high performance spectral code for nonlinear MHD stability. *Journal of Computational Physics*, 110(2):407–418, 1994.

[25] H. Weitzner. Ideal magnetohydrodynamic equilibrium in a non-symmetric topological torus. *Physics of Plasmas*, 21(2):022515, 2014.

[26] C. Zhu, D. A. Gates, S. R. Hudson, H. Liu, Y. Xu, A. Shimizu, and S. Okamura. Identification of important error fields in stellarators using the Hessian matrix method. *Nuclear Fusion*, 59(12):126007, 2019.